Downhole Receiver Function: a Case Study

by Kurang Mehta, Roel Snieder, and Vladimir Graizer

Abstract   Receiver function is defined as the spectral ratio of the radial component and the vertical component of the ground motion. It is used to characterize converted waves. We extend the use of the receiver function to downhole data using waves recorded in a borehole, excited by an earthquake of magnitude 4.0 near San Francisco, California, on 26 June 1994. The focal depth of the event was 6.6 km and the epicenter was located at a distance of 12.6 km from the borehole array. Six three-component sensors were located at different depths in a borehole. To extract a coherent response of the near-surface from the incoherent earthquake waves, we deconvolve the waves recorded by the sensors at different depths with the waves recorded by the sensor on the surface. Deconvolution applied to the waves in the S-time window recorded by the radial component result in an upgoing and a downgoing wave propagating with S-wave velocity. For the waves in the P-time window recorded by the radial component, deconvolution also gives an upgoing and a downgoing wave propagating with S-wave velocity. This interesting result suggests a P-to-S conversion at a depth below the deepest sensor. To diagnose this we compute the receiver function for the borehole recording of the earthquake waves. The receiver function shows an upgoing wave with an arrival close to time $t = 0$ for the deepest sensor. The agreement of the upgoing wave in the receiver function with the travel-time curve for the P-to-S converted wave, calculated using the P- and the S-wave velocity profile, supports the hypothesis of a pronounced P-to-S conversion. We present a synthetic example to illustrate that the first arrival of the receiver function applied to borehole data gives the upward-propagating P-to-S converted wave. To corroborate the observation of the mode conversion, we apply receiver function to a different earthquake data recorded by the same borehole array in 1998. The focal depth of the event was 6.9 km and the epicenter was located at a distance of 13 km from the borehole array. The receiver function for these data also show an upgoing wave with a pulse close to time $t = 0$ at the deepest sensor. The moveout of the upgoing wave agrees with the travel-time curve for the P-to-S converted wave, hence supporting our observation of the mode conversion.

Introduction

The receiver function, defined as the spectral ratio of the radial component and the vertical component, can be used to characterize converted waves (Phinney, 1964; Langston, 1977; Ammon, 1991; Sheehan *et al.*, 1995; Dueker and Sheehan, 1998; Ramesh *et al.*, 2002; Gilbert *et al.*, 2003; Wilson *et al.*, 2005). It is a powerful tool for producing discontinuity images of the crust and upper mantle from teleseismic earthquake arrivals (e.g., Wilson *et al.*, 2005). The ratio of the radial spectrum to the vertical spectrum depends on the structure beneath the surface (Phinney, 1964), notably in the presence of discontinuities. As the earthquake body waves travel through the earth, they produce a sequence of reflections, refractions, and conversions (e.g., P-to-S waves)

at discontinuities and/or rapid transition zones separating regions of differing seismic impedance. The receiver function emphasizes P-to-S converted phases from such interfaces while removing source complexity through the deconvolution of radial component seismograms by corresponding vertical component seismograms (Wilson *et al.*, 2005). Receiver functions are routinely used to obtain detailed crustal and upper mantle structure (e.g., Clouser and Langston, 1995).

Earthquake data recorded by the Treasure Island array (Graizer and Shakal, 2004) in the San Francisco Bay provided important information for studying local site effects (Graizer and Shakal, 2004). The array was installed in 1992

in an area that experienced liquefaction during the 1989 Loma Prieta earthquake. Graizer *et al.* (2000) and Graizer and Shakal (2004) analyzed these data to study site amplification effects as a function of depth. We apply seismic interferometry to the earthquake data to extract the near-surface 1D velocity profile. Seismic interferometry (Elgamal *et al.*, 1995; Haddadi and Kawakami, 1998; Lobkis and Weaver, 2001; Derode *et al.*, 2003; Kawakami and Oyunchimeg, 2003; Schuster *et al.*, 2004; Snieder, 2004; Wapenaar, 2004; Shapiro *et al.*, 2005; Wapenaar *et al.*, 2005; Curtis *et al.*, 2006; Snieder *et al.*, 2006) is a technique based on combining signals recorded at different sensors to estimate the response between them. Until recently, cross-correlation has been a widely used tool for applying seismic interferometry. Instead of cross-correlation, deconvolution can also be used as a seismic interferometric tool (Snieder and Şafak, 2006; Vasconcelos and Snieder, 2006). Deconvolution of the incoherent waveforms due to the earthquake recorded by the sensors at different depths in the borehole with the recording at the surface results in waves that propagate upward and downward along the array. These waves obtained by deconvolution can be used to estimate the 1D *P-* and *S*-wave velocity profiles. Further, we show the usefulness of receiver function applied to borehole data to diagnose the *P*-to-*S* converted wave.

Apart from the introduction, this article is divided into five sections. The second section describes the data recorded by the Treasure Island array after the earthquake in 1994. The waves obtained after deconvolution are shown in the third section. In the Receiver Function section we show the application of the receiver function to downhole data to understand the mode conversion. The fifth section illustrates the extension of receiver function to borehole data using a synthetic model. Finally, in the sixth section, we corroborate the observation of mode conversion using downhole receiver function for a different earthquake data recorded by the Treasure Island array in 1998.

Earthquake Data Recorded by Treasure Island Array

Downhole arrays have been installed by the California Strong Motion Instrumentation Program. A geotechnical downhole array of triaxial accelerometers, known as the Treasure Island array, was installed near San Francisco by California Strong Motion Instrumentation Program in cooperation with other agencies (Graizer *et al.*, 2000). This array was installed to study the response of soft sediments to ground motion (Graizer and Shakal, 2004). The array recorded waveforms excited by an earthquake on 26 June 1994 at 08:42:50.31 (UTC). The earthquake occurred near Richmond, California, and hence, in this article, is referred to as the Richmond earthquake. It was a magnitude 4.0 earthquake with focal depth of 6.6 km and epicenter 12.6 km from the borehole. The downhole array had six three-component sensors located at different depths with the deepest one at a depth of 104 m. Figure 1b shows the *P-* and the *S*-wave velocity profile down to the deepest sensor. The triangles indicate the location of the sensors. Figure 1a shows the radial component of the raw data. The data show initial compressional waves (*P*-waves) followed by shear waves (*S*-waves) and surface waves arriving at later times. In this article, we restrict our analysis to the body waves.

In the following section, we apply deconvolution to the waves in the *P-* and the *S*-time windows separately. Figure 1a shows the time windows used for gating the waves in the *P*-time window (1.0 to 4.5 sec) and the *S*-time window (4.5 to 15.0 sec) prior to deconvolution.

Deconvolution of the Recorded Waves

We use deconvolution as a tool for extracting the coherent response of the near-surface from incoherent earthquake waves recorded by the Treasure Island array. We first show deconvolution of the waveforms recorded by the vertical component of each sensor with the waveforms recorded
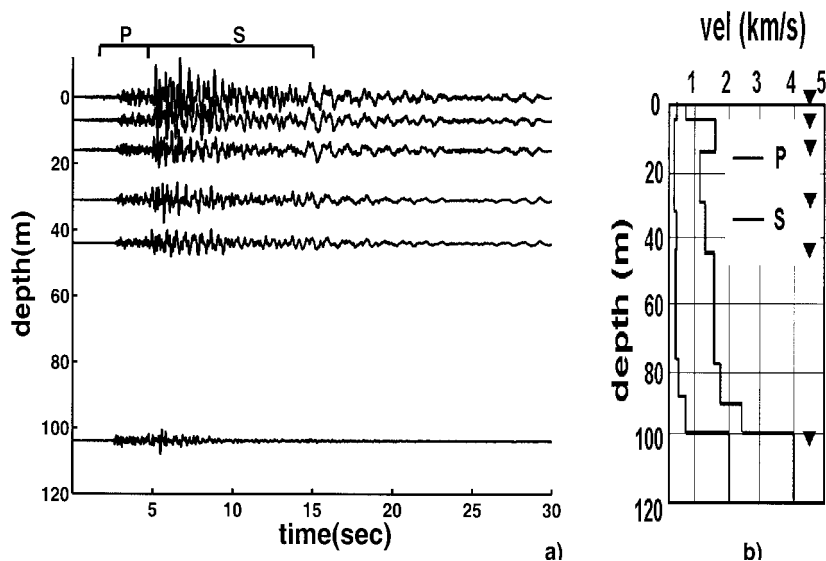

Figure 1. (a) The radial component of the ground motion recorded by the Treasure Island array near San Francisco during the Richmond earthquake in 1994. The array consists of six three-component sensors located at depths of 0, 7, 16, 31, 44, and 104 m. The time windows used for gating the *P* waves (1.0 to 4.5 sec) and the *S* waves (4.5 to 15.0 sec) is shown on the top. (b) The 1D velocity profile of the subsurface (Graizer and Shakal, 2004) down to 120 m. The triangles show the location of the sensors.

by the vertical component of the sensor on the surface ($z = 0$). The time domain data $u(z, t)$ is Fourier transformed into the frequency domain using $u(z, \omega) = \int u(z, t)e^{-i\omega t}dt$. The deconvolution of the resultant frequency domain data is given by

$$D(z, \omega) = \frac{u(z, \omega)}{u(z = 0, \omega)}. \qquad (1)$$

The deconvolution has poles at the zeros of the spectrum of $u(z = 0, \omega)$. To avoid this instability, we use a regularized deconvolution given by

$$D(z, \omega) = \frac{u(z, \omega)u^*(z = 0, \omega)}{|u(z = 0, \omega)|^2 + \varepsilon}, \qquad (2)$$

where the asterisk denotes complex conjugate and ε refers to a constant added at the denominator to prevent the instability of equation (1). For our analysis we choose ε to be 1% of the average spectral power of $u(z = 0, \omega)$. We then convert the frequency domain deconvolved waveforms (equation 2) into the time domain using $D(z, t) = \int D(z, \omega)e^{i\omega t}d\omega$.

The waves recorded in both the P- and the S-time window of the vertical component at each sensor location when deconvolved with those on the surface results in an upgoing and a downgoing wave (Fig. 2). The sloping dashed lines, representing the travel-time curve based on the P-wave velocity model of Graizer and Shakal (2004) (Fig. 1b), agree well with the upgoing and the downgoing waves inferred from the deconvolution. Hence, deconvolution applied to the waves recorded by the vertical component results in upgoing and downgoing waves propagating with the P-wave velocity.
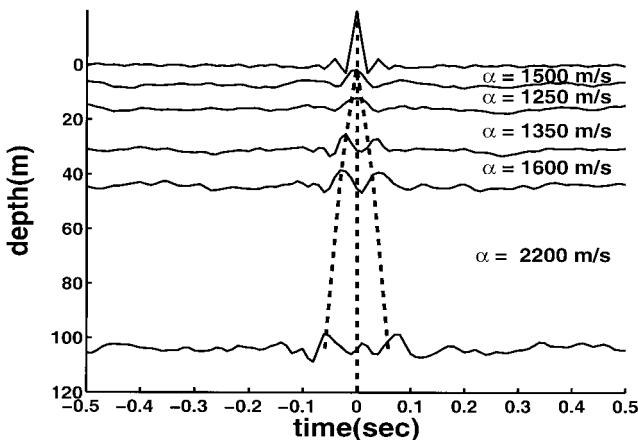

Figure 2.   Up- and downgoing waves obtained by deconvolving the waveforms recorded by the vertical component of each of the sensors with the waveforms recorded by the vertical component of the sensor on the surface (equation 2). The sloping dashed lines show the travel-time curve of the up- and the downgoing P waves computed from the P-wave velocity model from Graizer and Shakal (2004).

Similar to the vertical component, deconvolution of the waves recorded in the S-time window of the radial component at each of the sensors with the sensor on the surface results in an upgoing and a downgoing wave shown in Figure 3. The sloping dashed lines show the travel times for the upgoing and the downgoing S waves based on the S-wave velocity model of Graizer and Shakal (2004) shown in Figure 1b. These dashed lines, representing the S-wave travel-time curve, agree well with the upgoing and the downgoing waves inferred from the deconvolution. Mehta *et al.* (2007) established a connection of the deconvolved waveforms with the propagator matrix elements.

Figure 4 show the waveforms obtained after deconvolving the waves in the P-time window of the radial component at each sensor with the sensor on the surface. Instead of propagating with P-wave velocity, the deconvolved waves propagate with S-wave velocity. One possible explanation for this result is that, during the upward P-wave propagation, a P-to-S conversion occurs at a depth below the downhole array. The conversion would cause the waves before the primary S wave in Figure 1a to contain the P-to-S converted wave. The recordings in Figure 1a show that both the incoming P and S waves are incoherent. The lack of coherency is due to scattering along the path from the earthquake to the array. This scattering and the drastic variation in the velocity profile close to a depth of 100 m (Fig. 1b) leads to the mode conversion.

Because we have the recordings of both the radial and the vertical component at each of the sensors, we use the receiver function computed at each of the sensor location to diagnose the P-to-S mode conversion.

Receiver Function

We compute the receiver functions for the borehole recording of the earthquake waves to diagnose the upgoing P-to-S converted wave. The receiver function in a borehole is defined as the deconvolution of the waves recorded by the radial component at each of the sensor location with the waves recorded by the vertical component at the same sensor location. In the frequency domain, it is the spectral ratio of the radial component recorded at each of the sensor location in a borehole and the vertical component at the same sensor location, given by

$$R(z, \omega) = \frac{u_{\text{radial}}(z, \omega)}{u_{\text{vertical}}(z, \omega)}. \qquad (3)$$

The spectral ratio has poles at the zeros of the spectrum of $u_{\text{vertical}}(z, \omega)$. To avoid this instability, we use a regularized deconvolution given by

$$R(z, \omega) = \frac{u_{\text{radial}}(z, \omega)u^*_{\text{vertical}}(z, \omega)}{|u_{\text{vertical}}(z, \omega)|^2 + \varepsilon}. \qquad (4)$$

Park and Levin (2000) show that the receiver functions can also be computed by correlating the spectra of the radial
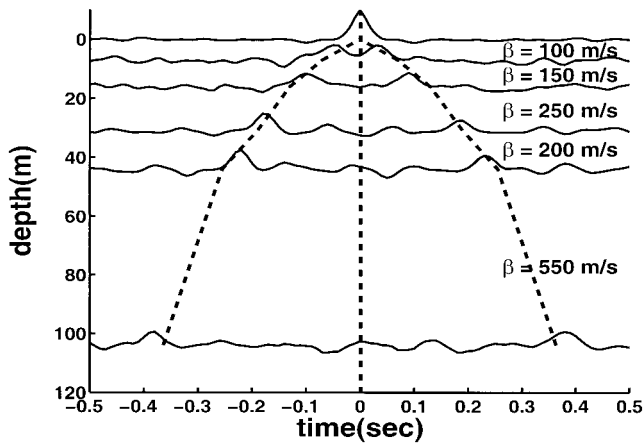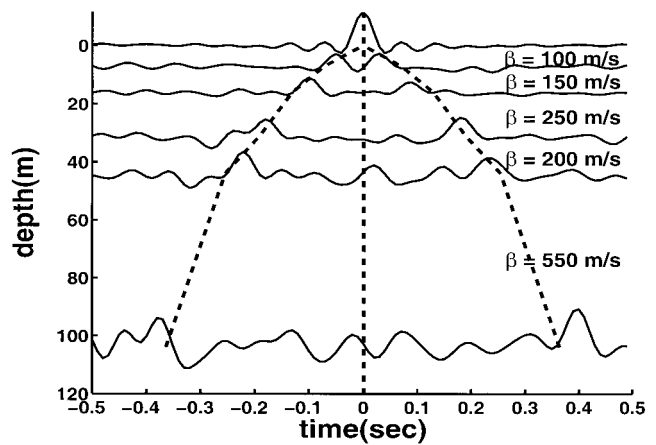
Figure 3. Up- and downgoing waves obtained by deconvolving the waveforms in the *S* window of the radial component of each of the sensors with the waveforms in the *S* window of the radial component of the sensor on the surface (equation 2). The sloping dashed lines show the travel-time curve of the up- and the downgoing *S* waves computed from the *S*-wave velocity model from Graizer and Shakal (2004).

Figure 4. Up- and downgoing waves obtained by deconvolving the waveforms in the *P* window of the radial component of each of the sensors with the waveforms in the *P* window of the radial component of the sensor on the surface (equation 2). The sloping dashed lines show the travel-time curve of the up- and the downgoing *S* waves computed from the *S*-wave velocity model from Graizer and Shakal (2004).

and the vertical component, rather than deconvolution. For nonnormal incidence, a simple rotation of radial and vertical components by the incidence angle is useful before applying the receiver function. The rotated coordinate system is referred to as the LQT coordinate system (Knapmeyer and Harjes, 2000). This rotation resolves the wave motion into a component normal to the *P* wavefront and a component parallel to the *P* wavefront. There could also be discrepancies in the orientation of the sensors. Yamazaki *et al.* (1992) demonstrated how such discrepancies in the orientation angles can be estimated.

For the Richmond earthquake, the incidence of the waves as recorded by the borehole sensors is close to normal; hence, we do not apply the rotation. In terms of discrepancies in the orientation angles, for the Treasure Island array installation of sensors in the borehole is done using special techniques to ensure proper orientation and leveling. Proper orientation is confirmed by comparing records at different depths.

We generate the receiver function at each sensor location by deconvolving the radial-component recording with the corresponding vertical-component recording. Figure 5 shows receiver functions computed at each sensor location for the downhole data. Each trace is the deconvolution of the waves recorded by the radial component at a given depth by the waves recorded by the vertical component at the same depth. The receiver functions show a distinct upgoing wave. The dashed line indicates the travel-time curve of the upgoing *P*-to-*S* converted wave calculated from the *P*- and the *S*-wave velocity model shown in Figure 1b (Graizer and Shakal, 2004), assuming a *P*-to-*S* conversion at a depth close to the deepest sensor (104 m). The agreement of the upgoing wave in the receiver function and this travel-time curve sup-
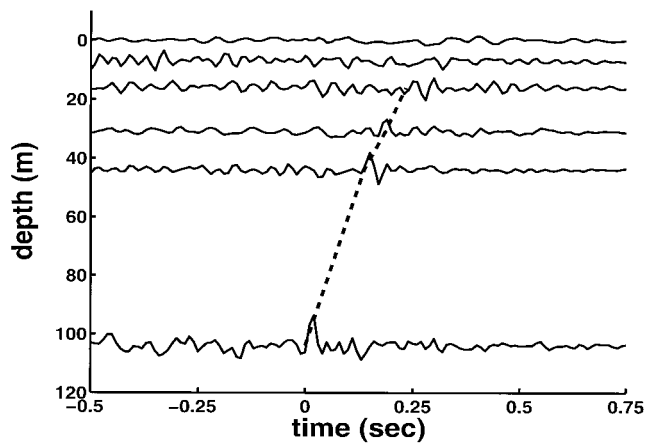

Figure 5. Receiver function, defined as the spectral ratio of the data recorded by the radial component with the data recorded by the vertical component at the same level. Each of the traces represents the deconvolution of the radial component at that specific sensor with the data recorded at the corresponding vertical component. The dashed line, computed from the *P*- and the *S*-wave velocity model of Graizer and Shakal (2004), shows the travel-time curve for a *P*-to-*S* converted wave with the conversion point just below the deepest sensor.

port the hypothesis of a pronounced *P*-to-*S* conversion. Arrival of the pulse close to time $t = 0$ at 104 m indicates that the conversion occurred very close the deepest sensor in the borehole. Graizer and Shakal (2004) show that the geology close to the depth of 100 m changes from unconsolidated sediments to Franciscan Bedrock Sandstone and Shale. The drastic variation in geology causes an increase in the *P*- and the *S*-wave velocity around this depth (as shown in Fig. 1b),

hence resulting in the strong mode conversion. The mode conversion due to the velocity variation occurs close to 100 m. Of six downhole sensors, five sensors are in the unconsolidated sediments (Fig. 1b), and hence, they sense the upgoing mode-converted wave generated at the interface of unconsolidated sediments and the Franciscan Bedrock Sandstone and Shale. The deepest sensor (104 m) is, however, very close below the interface (in the Franciscan Bedrock Sandstone and Shale) and the pulse arriving close to time $t = 0$ is possibly the upgoing P-wave that reflects as downgoing S-wave at the 100-m interface.

In the next section, we illustrate the use of receiver function to characterize upgoing P-to-S converted wave with a synthetic model.

Analysis Using Synthetic Model

The basic premise of receiver function is that the vertical component is a reasonable representation of the incident wave. A borehole recording contains not only the incident waves from the earthquake (upgoing waves) but also reflections off the free surface (downgoing waves). Hence, for the borehole sensors the receiver functions contain a complex series of phases with their timing and moveout determined by sensor depth and relative P- and S-wave travel times to the surface. The receiver function for a synthetic model is shown in Figure 6a. The model velocity profiles down to the deepest receiver (100 m) and down to the source depth (6000 m) are shown in Figure 6b and c, respectively. The source is at a horizontal distance of 1000 m from a borehole containing ten sensors spaced every 10 m starting from the surface.

To show that the first arrival in receiver function characterizes the P-to-S converted wave, we compute the receiver function for the synthetic model shown in Figure 6d. We assume borehole sensors from the surface ($z = 0$) down to $z = 100$ m spaced every 10 m.

The receiver function, in frequency domain, is given by

where

$$\phi_j > v_\beta(H - z), \qquad (6)$$
$$\psi_k > v_\alpha(H - z).$$

H is the depth of the conversion surface, v_β is the vertical wavenumber for S waves, and v_α is the vertical wavenumber for P waves. C_{ps} and C_{pp} are the P-S conversion coefficient and P-P transmission coefficient at the conversion surface. The first term of the receiver function (equation 5) characterizes the P-to-S converted wave (depicted by dashed line in Fig. 6a). The terms $A_j e^{i\phi_j}$ and $B_j e^{i\psi_j}$ denote waves that arrive after the P-to-S converted wave. Because the waves corresponding to terms $A_j e^{i\phi_j}$ and $B_j e^{i\psi_j}$ arrive at later times (as shown in Fig. 6a), the phase of these arrivals satisfies the inequalities in equation (6). The first square bracket in equation (5) represents the later-arriving phases containing the upgoing and the downgoing S waves present in the receiver function (Fig. 6a). The receiver function also contains the later phases propagating with the P-wave velocity. These waves are represented by the second square bracket in equation (5). The first arrival in the receiver functions applied to downhole data, however, characterizes the upgoing P-to-S converted wave and is highlighted by the dashed line. The moveout of the upgoing converted wave differs from the larger phases to follow. These larger phases mainly contain upgoing and downgoing P and S waves. The difference in the travel times for the converted wave as compared with that for the P and the S waves cause the discrepancy in the moveout. The receiver functions for the Richmond earthquake (Fig. 5) depicts the upgoing P-to-S converted wave. They do not, however, contain the later-arriving waves. The presence of strong attenuation due to soft unconsolidated sediments could be one possible reason for this observation.

Hence, the receiver function applied to borehole data contains a series of P and S waves given by equation (5).

$$
\begin{aligned}
\frac{u_x(z, \omega)}{u_z(z, \omega)} &= \frac{C_{ps}e^{iv_\beta(H-z)} + \sum_j A_j e^{i\phi_j}}{C_{pp}e^{iv_\alpha(H-z)} + \sum_k B_k e^{i\psi_k}} \\[2em]
&= \frac{C_{ps}e^{iv_\beta(H-z)}\left[1 + \dfrac{\sum_j A_j e^{i\phi_j}}{C_{ps}e^{iv_\beta(H-z)}}\right]}{C_{pp}e^{iv_\alpha(H-z)}\left[1 + \dfrac{\sum_k B_k e^{i\psi_k}}{C_{pp}e^{iv_\alpha(H-z)}}\right]} \\[2em]
&= \frac{C_{ps}}{C_{pp}} e^{i(H-z)(v_\beta - v_\alpha)}\left[1 + \frac{\sum_j A_j e^{i\phi_j}}{C_{ps}e^{iv_\beta(H-z)}}\right]\left[1 + \frac{\sum_k B_k e^{i\psi_k}}{C_{pp}e^{iv_\alpha(H-z)}}\right]^{-1}, \\[2em]
&= \frac{C_{ps}}{C_{pp}} e^{i(H-z)(v_\beta - v_\alpha)}\left[1 + \frac{\sum_j A_j e^{i\phi_j}}{C_{ps}e^{iv_\beta(H-z)}}\right]\left[\sum_{n=0}^{\infty}(-1)^n\left(\frac{\sum_k B_k e^{i\psi_k}}{C_{pp}e^{iv_\alpha(H-z)}}\right)^n\right],
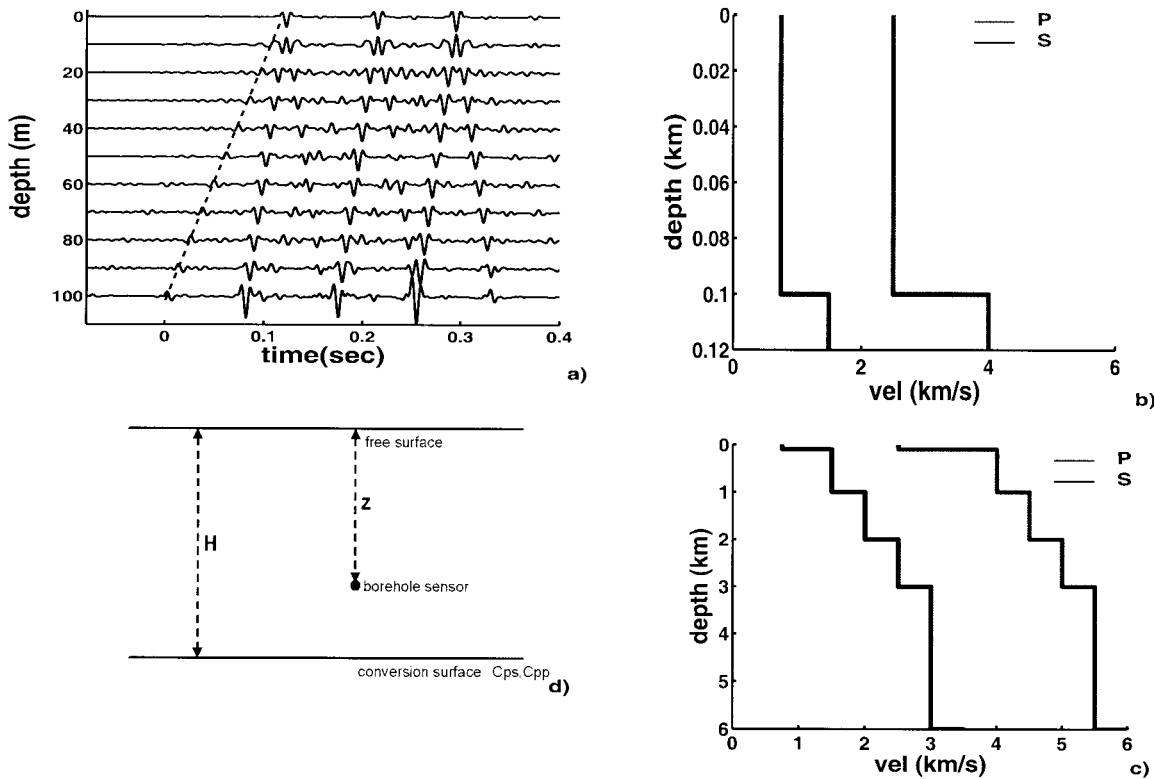\end{aligned}
\tag{5}
$$

Figure 6. (a) The receiver function computed for the synthetic model. The earlier arrival highlighted with the dashed line is the *P*-to-*S* converted wave. All the waves with other phases arrive at later times. (b) The velocity profile down 100 m. (c) The velocity profile down to the source depth (6000 m). (d) The cartoon of the model consisting of a homogeneous half-space above an interface at a depth *H*. Borehole sensors are located in the layer above the homogeneous half-space at a depth of *z* from the free surface. The conversion coefficients at the conversion surface are denoted as C_{ps} and C_{pp}.

The first arrival, however, represents the upgoing *P*-to-*S* converted wave.

Receiver Function Applied to Earthquake Data Recorded in 1998

We apply the receiver function to a different earthquake recorded by the Treasure Island array. The array recorded waveforms excited by an earthquake on 4 December 1998 at 12:16:07.8 (UTC). It was a magnitude 4.1 earthquake with focal depth of 6.9 km and epicenter 13 km from the borehole. The 1D *P*-wave and *S*-wave velocity profile and the sensor locations are shown in Figure 1b. The radial component of the raw data recording is shown in Figure 7. The *P* window (5.0 to 7.0 sec) and the *S* window (7.0 to 15.0 sec) used for windowing are shown on top of the plot.

The receiver function for the waveforms in the *P* window is shown in Figure 8. Similar to the Richmond earthquake data in 1994, the receiver functions show a distinct upgoing wave. The dashed line indicates the travel-time curve of the upgoing *P*-to-*S* converted wave calculated from the *P*- and the *S*-wave velocity model (Fig. 1b). The upgoing
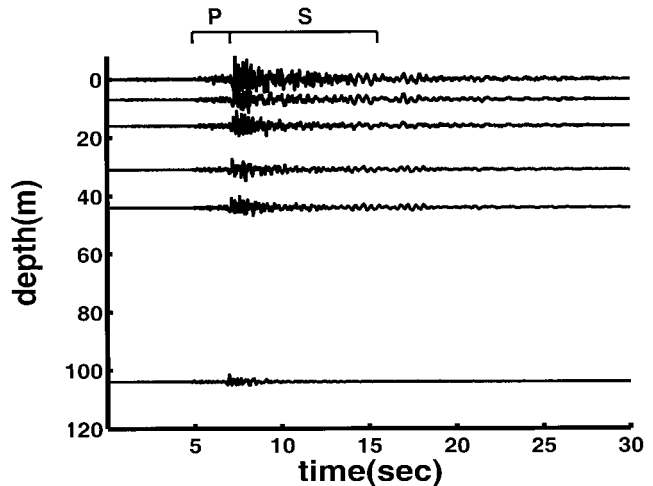

Figure 7. The radial component of the ground motion recorded by the Treasure Island array near San Francisco during an earthquake in 1998. The array consists of six three-component sensors located at depths of 0, 7, 16, 31, 44, and 104 m. The time windows used for gating the *P* waves (5.0 to 7.0 sec) and the *S* waves (7.0 to 15.0 sec) is shown on the top.
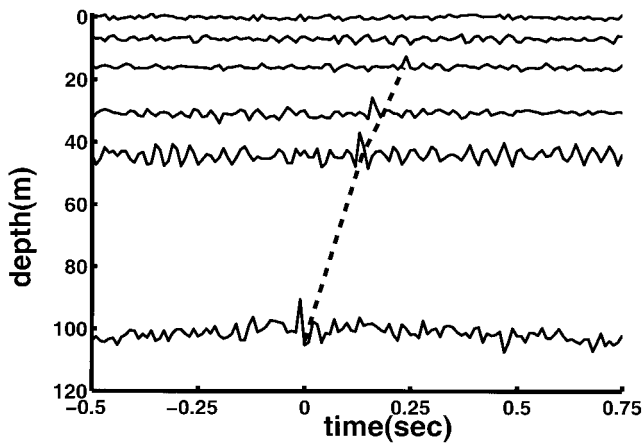
Figure 8. Receiver function computed for the earthquake in 1998. The dashed line, computed from the *P*- and the *S*-wave velocity model of Graizer and Shakal (2004), shows the travel-time curve for a *P*-to-*S* converted wave with the conversion point just below the deepest sensor.

wave in the receiver function agrees with this travel-time curve, hence supporting the observation of mode conversion using receiver function. Arrival of the pulse close to time $t = 0$ at 104 m depth indicates that the conversion occurred just below the deepest sensor in the borehole. Similar to the receiver function for the Richmond earthquake data, the later phases are not present in the receiver function due to strong attenuation in the near-surface.

Conclusion

We observe *P*-to-*S* mode conversion when deconvolution is applied to the waves in the *P* window of the radial component. Deconvolution applied to the waves in the *P* window of the radial component results in an upgoing and a downgoing wave propagating with the *S*-wave velocity. This is possible when the arrivals before the primary *S* wave contain *S* waves generated by *P*-to-*S* mode conversion. Receiver function applied to two downhole data sets support this observation of the mode conversion just below the deepest sensor in the borehole. Analysis using a synthetic example illustrates that the first arrival of the receiver function applied to borehole data gives an upgoing *P*-to-*S* converted wave.

Acknowledgments

References

Ammon, C. J. (1991). The isolation of receiver effects from teleseismic P waveforms, *Bull. Seism. Soc. Am.* **81,** no. 6, 2504–2510.

Clouser, R. H., and C. A. Langston (1995). Effect of sinusoidal interfaces on teleseismic P-wave receiver functions, *Geophys. J. Int.* **123,** 541–558.

Curtis, A., P. Gerstoft, H. Sato, R. Snieder, and K. Wapenaar (2006). Seismic interferometry—turning noise into signal, *The Leading Edge* **25,** 1082–1092.

Derode, A., E. Lacrose, M. Campillo, and M. Fink (2003). How to estimate the Green's function for a heterogeneous medium between two passive sensors? Application to acoustic waves, *Appl. Phys. Lett.* **83,** 3054–3056.

Dueker, K. G., and A. F. Sheehan (1998). Mantle discontinuity structure beneath the Colorado Rocky Mountains and High Plains, *J. Geophys. Res.* **103,** 7153–7169.

Elgamal, A. W., M. Zeghal, H. T. Tang, and J. C. Stepp (1995). Lotung Downhole Array, I: Evaluation of site dynamic properties, *J. Geotech. Eng.* **121,** no. 4, 350–362.

Gilbert, H. J., A. F. Sheehan, K. G. Dueker, and P. Molnar (2003). Receiver functions in the western United States, with implications for upper mantle structure and dynamics, *J. Geophys. Res.* **108,** no. B5, 2229, doi 10.1029/2001JB001194.

Graizer, V., and A. Shakal (2004). Analysis of some of CSMIP strong-motion geotechnical array recordings, presented at Proceedings of the International Workshop for Site Selection, Installation and Operation of Geotechnical Strong-Motion Arrays: Workshop 1, Inventory of Current and Planner Arrays, 14 and 15 October 2004, COSMOS, SCEC, and USC.

Graizer, V., T. Cao, A. Shakal, and P. Hipley (2000). Data from downhole arrays instrumented by the California Strong Motion Instrumentation Program in studies of site amplification effects, presented at the Proceedings of the 6th International Conference on Seismic Zonation, Palm Springs, California.

Haddadi, H. R., and H. Kawakami (1998). Characteristics of Vertical Component Strong Ground Motion by NIOM (Normalized Input-Output Minimization) Method, in *Proc. of 10th Japan Symposium of Earthquake Engineering*, 1187–1192.

Kawakami, H., and M. Oyunchimeg (2003). Normalized input-output minimization analysis of wave propagation in buildings, *Eng. Struct.* **25,** 1429–1442.

Knapmeyer, M., and H. Harjes (2000). Imaging crustal discontinuities and the downgoing slab beneath western Crete, *Geophys. J. Int.* **143,** 1–21.

Langston, C. A. (1977), Corvallis, Oregon, crustal and upper mantle receiver structure from teleseismic P-waves and S-waves, *Bull. Seism. Soc. Am.* **67,** 713–724.

Lobkis, O. I., and R. L. Weaver (2001). On the emergence of the Green's function in the correlations of a diffuse field, *J. Acoust. Soc. Am.* **110,** 3011–3017.

Mehta, K., R. Snieder, and V. Graizer (2007). Extraction of near-surface properties for a lossy layered medium using the propagator matrix, *Geophys. J. Int.* **169,** 271–280.

Park, J., and V. Levin (2000). Receiver functions from multiple-taper spectral correlation estimates, *Bull. Seism. Soc. Am.* **90,** 1507–1520.

Phinney, R. A. (1964). Structure of the Earth's crust from spectral behavior of long-period body waves, *J. Geophys. Res.* **69,** no. 14, 2997–3017.

Ramesh, D. S., R. Kind, and X. Yuan (2002). Receiver function analysis of the North American crust and upper mantle, *Geophys. J. Int.* **150,** 91–108.

Schuster, G. T., J. Yu, J. Sheng, and J. Rickett (2004). Interferometric/daylight seismic imaging, *Geophys. J. Int.* **157,** 838–852.

Shapiro, N. M., M. Campillo, L. Stehly, and M. H. Ritzwoller (2005). High-resolution surface-wave tomography from ambient seismic noise, *Science* **307,** 1615–1618.

Sheehan, A. F., G. A. Abers, C. H. Jones, and A. L. Lerner-Lam (1995).

Crustal thickness variations across the Colorado Rocky Mountains from teleseismic receiver functions, *J. Geophys. Res.* **100,** 20,391–20,404.

Snieder, R. (2004). Extracting the Green's function from the correlation of coda waves: a derivation based on stationary phase, *Phys. Rev. E.* **69,** 046610.

Snieder, R., and E. Şafak (2006). Extracting the building response using seismic interferometry: theory and application to the Millikan Library in Pasadena, California, *Bull. Seism. Soc. Am.* **96,** no. 2, 586–598.

Snieder, R., K. Wapenaar, and K. Larner (2006). Spurious multiples in interferometric imaging of primaries, *Geophysics* **71,** SI65–SI78.

Vasconcelos, I., and R. Snieder (2006). Interferometric imaging by deconvolution: theory and numerical examples, *SEG Expanded Abstracts* **25,** 2416–2419.

Wapenaar, K. (2004). Retrieving the elastodynamic Green's function of an arbitrary inhomogeneous medium by cross-correlation, *Phys. Rev. Lett.* **93,** 254301.

Wapenaar, K., J. Fokkema, and R. Snieder (2005). Retrieving the Green's function by cross-correlation: a comparison of approaches, *J. Acoust. Soc. Am.* **118,** 2783–2786.

Wilson, D., R. Aster, J. Ni, S. Grand, M. West, W. Gao, W. S. Baldridge, and S. Semken (2005). Imaging the seismic structure of the crust and upper mantle beneath the Great Plains, Rio Grande Rift, and Colorado Plateau using receiver functions, *J. Geophys. Res.* **110,** B05306, doi 10.1029/2004JB003492.

Yamazaki, F., L. Lu, and T. Katayama (1992). Orientation error estimation of buried seismographs in array observation, *Earthquake Eng. Struct. Dyn.* **21,** 679–694.

Center for Wave Phenomena, Department of Geophysics
Colorado School of Mines
Golden, Colorado 80401
  (K.M., R.S.)

California Geological Survey
Sacramento, California 95814
  (V.G.)